arXiv:cond-mat/0507458v1 [cond-mat.dis-nn] 19 Jul 2005

Finite-Connectivity Spin-Glass Phase Diagrams and Low Density Parity Check Codes

Gabriele Migliorini and David Saad
The Neural Computing Research Group
School of Engineering and Applied Sciences, Aston University
Birmingham B4 7ET, United Kingdom.

We obtain phase diagrams of regular and irregular finite connectivity spin-glasses. Contact is firstly established between properties of the phase diagram and the performances of low density parity check codes (LDPC) within the Replica Symmetric (RS) ansätz. We then study the location of the dynamical and critical transition of these systems within the one step Replica Symmetry Breaking theory (RSB), extending similar calculations that have been performed in the past for the Bethe spin-glass problem. We observe that, away from the Nishimori line, in the low temperature region, the location of the dynamical transition line *does* change within the RSB theory, in comparison with the (RS) case. For LDPC decoding over the binary erasure channel we find, at zero temperature and rate $R = 1/4$ an RS critical transition point located at $p_c \simeq 0.67$ while the critical RSB transition point is located at $p_c \simeq 0.7450 \pm 0.0050$, to be compared with the corresponding Shannon bound $1 - R$. For the binary symmetric channel (BSC) we show that the low temperature reentrant behavior of the dynamical transition line, observed within the RS ansätz, changes within the RSB theory; the location of the dynamical transition point occurring at higher values of the channel noise. Possible practical implications to improve the performances of the state-of-the-art error correcting codes are discussed.

PACS numbers: 89.90+n, 89.70+c,05.50+q

I. INTRODUCTION

The survival of ferromagnetic ordering under the disruption of frozen random fields [1] and the onset of Spin-Glass (SG) order in systems characterized by random competing interactions [2] are two central problems in the statistical mechanics of systems with quenched randomness. When properly rephrased, these two problems turn out to relate to core problems in other, quite different disciplines. Insight into these two closely related problems in any given system is obtained from the corresponding phase diagram as a function of the physical parameters, such as temperature and disorder strength.

Finite-connectivity mean-field SG models [3, 4, 5, 6, 7] and their p-spin counterpart [8] are important for two distinct reasons. Firstly, despite being mean-field in nature, they are believed to share common properties with finite-dimensional spin-glass systems [9, 10]. Secondly, the statistical mechanics of SG model systems with fixed finite connectivity relates to the study of various hard computational problems. In the last two decades the analysis of finite-connectivity SG systems has also offered new tools for understanding the very nature of several optimization problems *and* improve algorithmic performances [11, 12]. In this paper we first obtain the phase diagram of finite-connectivity mean-field SG models. We then investigate the relation between features of the phase diagram and the performance of Low Density Parity Check (LDPC) Codes, analyzing the effects induced by the Replica Symmetry Breaking (RSB) nature of solutions obtained for these finite-connectivity SG models [13]. In order to answer these questions, we exploit the relation between finite-connectivity SG systems and a class of exactly solvable models; we employ an efficient computational method that has been shown to be quite effective for understanding several features of finite-dimensional SG [14].

We will consider a generalized model unifying the frameworks for a few distinct problems.

Particular attention will be given to two special cases: a) The Bethe SG which has been extensively studied under both Replica Symmetric (RS) and RSB ansätze [3, 4, 5] and recently considered in its ferromagnetically biased version [15]. b) Gallager (LDPC) error-correcting codes [16]. While the former is well known within the statistical physics community, many in this community are less familiar with the latter and its links to the physics of disordered systems.

Reliable transmission of information in noisy conditions is one of the basic problems of modern communication technology. Correspondingly, one of the central problems of information theory is channel coding. Methods to achieve reliable information transmission rely on the introduction of structured redundancy to the original message in order to compensate for corruption due to noise. Shannon derived rigorous bounds on the level of redundancy (the code rate) required to enable error-free communication for a given channel noise [17]. However, Shannon's theorems are non-constructive and do not offer a practical coding scheme. Different methods, based on various redundancy construction recipes, have been proposed over the years [18]. Despite the fact that error-correcting codes are now widely used in a variety of applications, current performances of most methods are significantly below Shannon's bound. One family of error-correcting codes that have been shown to provide close-to-optimal performances is that of Gallager's LDPC

codes [16]. In these codes the structured redundancy is introduced through parity checks of Boolean sums of randomly sampled message bits. The relation between the parity-check error-correcting codes and SG models, and consequently between quite different disciplines as statistical physics and information theory, has been pointed to in the seminal work of Sourlas [19].

Decoding in LDPC codes corresponds to a class of SG models defined by an underlying lattice geometry that reflects the low density character of the code construction. The importance of this very last point, that made the above correspondence useful and of practical relevance was not understood until recently [20]. Methods developed in the statistical mechanics of diluted SG under the RS ansätz have been successfully employed to compute macroscopic properties of such systems for different parameter values; reasonable agreement with observed decoding bounds have been reported [21]. To our knowledge however, the only phase diagram that has been evaluated for LDPC codes is in the limit of large coordination/large multi-spin interaction numbers [22], which also relates to the phase diagram of the Random Energy Model (REM) [23].

In the following section we introduce the class of Ising spin systems to be analyzed and its links to the Bethe SG and LDPC decoding problems. This will be followed by section III where we review the RS equations and the corresponding solutions are obtained using a computational method adopted from the study of d-dimensional hierarchical models. As part of this section we will present the method and briefly discuss the relation between finite-connectivity SG and d-dimensional hierarchical models. In section IV we introduce the equations behind the RSB theory of finite-connectivity SG studied here and present results obtained for the Bethe SG problem and LDPC error-correcting codes under two different transmission channels: the binary erasure channel (BEC) and the binary symmetric channel (BSC). In section V we discuss the results obtained and point to future research directions.

II. THE MODEL

The two different models examined in this work stem from a unified physical system of K-spin interaction Ising model on a lattice of fixed connectivity C. The Hamiltonian describing the system takes the form

$$\mathcal{H}_0 = -J \sum_{\mu} \mathcal{A}_{\mu} \prod_{i \in \mathcal{L}(\mu)} S_i \ , \tag{1}$$

where $\boldsymbol{S} \in \{\pm 1\}^N$ represents N binary variables, $\mathcal{L}(\mu) = \langle i_1, \ldots, i_K \rangle$ a set of indices related to interaction μ and $\mathcal{A}_{\mu}$ the corresponding connectivity tensor with the following properties:

$$\begin{aligned} \mathcal{A}^{\mu}_{\langle i_1,\ldots,i_K \rangle} &= \begin{cases} 1 & \text{for} \quad \mathcal{L}(\mu) = \langle i_1, \ldots i_K \rangle \\ 0 & \text{otherwise} \end{cases} \\ \sum_{\langle i_2,\ldots,i_K \rangle} \mathcal{A}_{\langle i,i_2,\ldots,i_K \rangle} &= C \quad \forall i \ . \end{aligned} \tag{2}$$

The parameter J is related to the strength of the random exchange interaction.

The various models considered in this work differ in the connectivity parameters and type of bias used, which corresponds to an additional component of the Hamiltonian (1).

A. The Bethe SG

The Bethe SG has been extensively studied in the past [3, 4, 5] and represents a special case of the Hamiltonian (1) where one is only considering pairwise interactions, $K = 2$.

Bethe SG with ferromagnetically biased exchange interaction J, which we will focus on here, has been recently studied in [15], where the distribution of the quenched random variable J takes the form

$$P(J) = \frac{1+\rho}{2} \ \delta(J-1) + \frac{1-\rho}{2} \ \delta(J+1) \ , \tag{3}$$

and where the parameter $\rho \in [0,1]$ is $\rho = 1$ for a ferromagnet and $\rho = 0$ for the unbiased Bethe SG.

B. LDPC error-correcting codes

We consider a simple communication model whereby L bit messages are encoded using LDPC codes and then communicated through two channel types: *a*) The Binary Symmetric Channel (BSC) where bits are flipped with probability p during transmission and *b*) The Binary Erasure Channel (BEC) where bits are received with probability $1-p$ and fail to arrive with probability p.

A Gallager LDPC code is defined by a binary matrix $\boldsymbol{H} = [\boldsymbol{A} \mid \boldsymbol{B}]$, concatenating two very sparse matrices known to both sender and receiver, with $\boldsymbol{B}$ (of dimensionality $(N-L) \times (N-L)$) being invertible; the matrix $\boldsymbol{A}$ is of dimensionality $(N-L) \times L$. LDPC codes can be employed over various finite fields [24]; we will restrict the treatment in this paper to binary symbols.

Encoding refers to mapping the original L dimensional binary message vector $\boldsymbol{\xi} \in \{0,1\}^L$ to an N dimensional binary code word $\boldsymbol{t} \in \{0,1\}^N$ $(N > L)$ by taking the product $\boldsymbol{t} = \boldsymbol{G^T \xi} \pmod 2$, where all operations are performed in the field $\{0,1\}$ and are indicated by (mod 2). The generator matrix is $\boldsymbol{G^T} = [\boldsymbol{I} \mid (\boldsymbol{B^{-1}A})^T] \pmod 2$, where $\boldsymbol{I}$ is the $L \times L$ identity matrix, implying that $\boldsymbol{HG^T} \pmod 2 = 0$ and that the first L bits of $\boldsymbol{t}$ are set to the message $\boldsymbol{\xi}$. In *regular* Gallager codes the number of non-zero elements in each row of $\boldsymbol{H}$ is chosen to

be exactly K. The number of elements per column is then $C = (1-R)K$, where the code rate is $R = L/N$ (for unbiased messages). We will mostly focus here on regular code constructions.

1. BSC

The corruption process that is most intuitively linked to physical systems is the BSC, where the encoded vector $\boldsymbol{t}$ is corrupted by flip noise represented by the vector $\boldsymbol{\zeta} \in \{0,1\}^L$ with components independently drawn from $P(\zeta) = (1-p)\ \delta(\zeta) + p\ \delta(\zeta - 1)$. The received vector takes the form $\boldsymbol{r} = \boldsymbol{G^T}\boldsymbol{\xi} + \boldsymbol{\zeta}$ (mod 2).

Decoding is carried out by multiplying the received message by the matrix $\boldsymbol{H}$ to produce the *syndrome* vector $\boldsymbol{z} = \boldsymbol{H}\boldsymbol{r} = \boldsymbol{H}\boldsymbol{\zeta}$ (mod 2) from which an estimate $\widehat{\boldsymbol{\zeta}}$ for the noise vector can be inferred. An estimate for the original message is then obtained as the first L bits of $\boldsymbol{r} + \widehat{\boldsymbol{\zeta}}$ (mod 2).

The Bayes optimal estimator (also known as *Marginal Posterior Maximiser* (MPM)) for noise vector bits is defined as $\widehat{\zeta}_j = \text{argmax}_{S_j} P(S_j \mid \boldsymbol{z})$. Computing the MPM estimate directly is computationally hard, and is typically approximated in practice by employing an iterative inference algorithm such as belief propagation [25].

The connection to statistical physics becomes clear when the field $\{0,1\}$ is replaced by Ising spins $\{\pm 1\}$ and mod 2 sums by products [19]. The syndrome vector acquires the form of a multi-spin coupling $\mathcal{J}_\mu = \prod_{i\in\mathcal{L}(\mu)} \zeta_i$ where $i = 1,\dots,N$ and $\mu = 1,\dots,(N-L)$. The K indices of nonzero elements in the row μ of $\boldsymbol{A}$ are given by $\mathcal{L}(\mu) = \{i_1,\dots,i_K\}$ and where $\mathcal{A}_{\langle i_1,\cdots i_K\rangle}$ is the connectivity tensor is given in equation (2). After gauging $S_j \to S_j\zeta_j$ the multi-spin coupling coefficient vanishes ($\mathcal{J}_\mu = 1$) and the parity check component of the Hamiltonian takes the form (1) with $J \to \infty$ forcing all candidate vectors to obey the parity checks. This notation is used to distinguish the temperature from the parity check constraints and to facilitate the finite temperature study of error-correcting codes.

Prior knowledge of the biased noise vector is added through a second component to the Hamiltonian (1). After gauging, the new term takes the form $H_1 = -F\sum_{j=1}^N S_j\zeta_j$ where $F = \frac{1}{2}\log(\frac{1-p}{p})$ is the Nishimori condition [26, 27] (where $\beta = 1$), which corresponds to the correct prior for the variables $\boldsymbol{S}$. Decoding at the Nishimori condition corresponds to the MPM estimation [28]. This gives rise to the Hamiltonian

$$-\beta\mathcal{H} = \beta J \sum_\mu \mathcal{A}_\mu \prod_{i\in\mathcal{L}(\mu)} S_i + \beta F \sum_{j=1}^N S_j\zeta_j\ , \qquad (4)$$

for the BSC.

Another important estimator one should mention is the *Maximum A Posteriori* (MAP) estimator defined as $\widehat{\boldsymbol{\zeta}} = \text{argmax}_{\boldsymbol{S}} P(\boldsymbol{S} \mid \boldsymbol{z})$. This corresponds to zero temperature decoding [28].

2. BEC

Codeword bits transmitted over a BEC have a probability $1-p$ of being received (in tact). Encoding is carried out similarly to the BSC, but decoding is based on inferring the codeword itself, rather than the noise vector.

In the case of the BEC, solution vectors are, by definition, codewords and should therefore obey $\boldsymbol{H}\boldsymbol{S}$ (mod 2) $= 0$, where $\boldsymbol{S}$ are the received vectors (with a certain number of unknown bits).

An estimate of the original message is then obtained by inferring the missing bits using MPM. Similar practical methods to those described in the BSC may be employed also in this case.

The statistical mechanics formulation of the problem is similar to that of the BSC, except for the second component added to the Hamiltonian (1), that takes the form

$$H_1 = -\sum_{i=1}^N \ln\left[p + (1-p)\prod_i \delta_{S_i,1}\right]\ . \qquad (5)$$

Code performance in the BEC will be considered only at the zero temperature limit as in [29].

A review of LDPC codes and their link to statistical mechanics has been presented in [30].

III. REPLICA SYMMETRIC THEORY

The analysis carried out here is a natural extension of similar calculations done in the past for the Bethe SG [31] model and p-spin Ising models [3]. We therefore briefly review the RS theory of the model described by Hamiltonian (4) as both the Bethe SG and LDPC decoding can be considered as special cases of the same model.

To compute the free energy of the problem, consider the replica equality,

$$\beta f = -\lim_{N\to\infty} \frac{1}{N}\frac{\partial}{\partial n}\Big|_{n\to 0} \langle \mathcal{Z}^n\rangle_{\mathcal{A},\zeta,J}, \qquad (6)$$

where $\langle \mathcal{Z}^n\rangle_{\mathcal{A},\zeta,J}$ is the analytical continuation in the interval $n \in [0,1]$ of the replicated partition function [33]. Following the standard derivation, e.g. as in [21, 34], and employing the RS ansätz, one obtains the following expression for the replica symmetric free-energy as a function of the local field distribution $\pi(x)$ (details can be found in Appendix A)

$$\beta f = \Delta f^{(1)} - C\frac{K-1}{K}\Delta f^{(2)}. \qquad (7)$$

There are both site and bond contributions,

$$\Delta f^{(1)} = -E_{J,\zeta} \int \prod_{j=1}^{C} \prod_{j'=1}^{K-1} dx_{jj'}\ \pi(x_{jj'})\ \mathcal{F}^{(1)}(\{x_{jj'}\},\zeta,J_j)$$
$$\Delta f^{(2)} = -E_J \int \prod_{j=1}^{K} dx_j\ \pi(x_j)\ \mathcal{F}^{(2)}(\{x_j\},J_j), \quad (8)$$

where $E_{J,\zeta}$ denotes an average over the two sources of randomness in (4), and

$$\mathcal{F}_a^{(1)} = \log 2\cosh\beta\Big(\sum_j u(\{x_{jj'}\},J_j) + F\zeta\Big)$$
$$\mathcal{F}_b^{(1)} = a(\{x_{jj'}\},J_j),$$
$$\mathcal{F}^{(2)} = a(\{x_j\},J_j) + u(\{x_j\},J_j)\ . \quad (9)$$

We denote $\mathcal{F}^{(1)} = \mathcal{F}_a^{(1)} + \mathcal{F}_b^{(1)}$ where

$$\beta u(\{x_j\},J) = \frac{1}{2}\log[R(+)/R(-)]$$
$$\beta a(\{x_j\},J) = \frac{1}{2}\log[R(+)R(-)]\ . \quad (10)$$

The polynomials $R(\sigma)$ are defined via,

$$R(\sigma) = \sum_{\sigma_1,\cdots\sigma_{K-1}} \exp\beta[y_1\sigma\sigma_1 + y_2\sigma_1\sigma_2 + \cdots y_K\sigma_{K-1}\sigma], \quad (11)$$

where $\{y_1,\cdots,y_K\} \equiv \{x_1,\cdots x_{K-1},J\}$. The above expression, in a similar form, has already been obtained in [20], and the equivalence with their expression is shown in Appendix A. We prefer the current formulation because of its manifest simplicity (the two contributions to the free-energy coming from sites and bonds are here in evidence) and because it depends on the function $a(\{x_j\},J_j)$, which will play a central role in the RSB case, examined in section IV.

The above writing also introduces the polynomials $R(\sigma)$, already well known in the context of hierarchical lattices [14]. Evaluating the saddle point equations of the above free-energy expression is the basic premise of the RS theory, so that the crux of the quenched randomness problem (4) lies in the convolution [20],

$$\pi(x) = E_{J,\zeta} \int \prod_{ij} dx_{ij}\ \pi(x_{ij})\ \delta\Big(x - \mathcal{R}(\{x_{ij}\},J,\zeta)\Big), \quad (12)$$

where $i = 1,\cdots,C-1$, $j = 1,\cdots,K-1$; and where the recursion relations are defined via

$$\mathcal{R}(\{x_{ij}\},J,\zeta) = \sum_{j=1}^{C-1} u(\{x_{ij}\},J_j) + F\zeta\ . \quad (13)$$

We can also rewrite for convenience the above convolution with the aid of the auxiliary distribution $\hat{\pi}(\hat{x})$, as a set of two coupled equations (cfr. Appendix A),

$$\pi(x) = E_\zeta \int \prod_{i=1}^{C-1} d\hat{x}_i\ \hat{\pi}(\hat{x}_i)\ \delta\Big(x - \sum_{i=1}^{C-1}\hat{x}_i - F\zeta\Big)$$
$$\hat{\pi}(\hat{x}) = E_J \int \prod_{j=1}^{K-1} dx_j\ \pi(x_j)\ \delta\Big(\hat{x} - u(\{x_j\},J)\Big). \quad (14)$$

A. Saddle Point Equations and LDPC Decoding

To briefly explain the link between LDPC decoding and the replica formulation we will restrict this discussion to the BSC. The replica analysis as well as decoding in other noisy channels follow a similar path [35].

Following the derivation of [21] we write saddle point equations for the LDPC decoding problem, considering a special case of the Hamiltonian (4) and the saddle point equations (14), where $J \to \infty$ is deterministic

$$\pi(x) = E_\zeta \int \prod_{i=1}^{C-1} d\hat{x}_i\ \hat{\pi}(\hat{x})\ \delta\Big(x - \sum_{i=1}^{C-1}\hat{x}_i - F\zeta\Big)$$
$$\hat{\pi}(\hat{x}) = \int \prod_{j=1}^{K-1} dx_j\ \ pi(x_j)\ \delta\Big(\hat{x} - u_\beta(\{x_j\})\Big)\ . \quad (15)$$

Most of the numerical results obtained so far are obtained along the Nishimori line $\beta = 1$. Here we investigate the phase diagram at *any* prior temperature $1/\beta F$, for different choices of the parameters C and K. A typical case we will discuss in detail is the one corresponding to $C = 3$, $K = 4$.

We will check the consistency between the results obtained and true decoding experiments, using Belief Propagation (BP) [36], at and away from the Nishimori condition. We will not review BP in the paper as it is a well known message passing algorithm [25, 37] with strong links to the Bethe approximation and its variants [38, 39]. The iterative algorithm is a microscopic equivalent of equations (15).

B. The Computational Method

The set of (RS) equations (14) have been considered and solved in a variety of different ways already. This section introduces to a different method. We propose an alternative approach to existing methods (e.g. population dynamics or Monte Carlo techniques) which solves equations of the form (12) efficiently and accurately. The main reason why it has not been used to study finite-connectivity SG models so far is because of the different context in which it was firstly introduced [40]. The method we propose allows to determine the phase diagram of diluted systems of the type studied here and analyze the nature and exact location of the phase boundaries. It borrows tools and concepts from a different

branch of research, namely the area of hierarchical models [14, 41], to obtain accurate phase diagrams. The iterative method we now describe has a corresponding computational effort that scales as N^{K-1}, N being the number of bins introduced and K the multi-spin interaction parameter.

Equation (12) complicates, after a few iterations, even a simple initial local field distribution. The distribution $\pi(x)$ and its conjugate distribution $\hat{\pi}(\hat{x})$ are represented via histograms. Each histogram is characterized by two quantities, x_{ij} and $\pi(x)$, where the latter is the associated probability. Equation (15) is the convolution of $(K-1)C$ distributions, taking into account the distribution of the random field $P(\zeta)$, contained in the average $E_\zeta(..) = \int P(\zeta)d\zeta(..)$. This is numerically constructed from pairwise convolutions of distributions. For a $R = 1/4$ rate Gallager code , e.g., three pairwise convolutions are required. A pairwise convolution (or binary operation) is achieved as follows:
(1) The histograms are placed on a grid properly drawn at each iteration step of the algorithm. All histograms that fall within the same grid cell are combined in such a way as to preserve the averages across the domain of the local field (and its conjugated) distribution(s). The histograms that falls outside the grid, representing a predetermined small fraction of the overall probability, are similarly combined into a single histogram. In this procedure, a histogram that falls within a narrow band of a grid boundary is proportionally shared between neighboring bins. The gridding is done separately for $x > 0$ and $x < 0$.
(2) Two gridded distributions are convoluted according to equation (14) regenerating the original number of histograms.
The convolution of $C(K-1)$ distributions is achieved, from pairwise convolutions, as follows: (1) The pairwise convolution contained in the first equation of (14) is cycled once for, e.g., a code rate $R = 1/4$. (2) The resulting distribution is pairwise-convoluted with the noise channel distribution $P(\zeta)$. (3) The resulting distribution is further self-convoluted according to the second equation in (14). This completes the entire process, that is then iterated until convergence is achieved. Multiple cycling operations are also an interesting option being related to, e.g., the source compression problem. The flows of the probability distribution $\pi(x)$ determine the phase diagram of the system. Most of our results have been obtained considering 125×4 independent bins, corresponding to the flows of 10^3 quantities (the corresponding number of elementary operations considered is the number of bins to the power of $K-1$). Each of the two grids at $x > 0$ and $x < 0$ have e.g. 125 bins on each side of the average value.
Similar set of equations to (12) have been discussed in a variety of different contexts. A very important one is that of real-space renormalization-group theory [40] [41] [42].

Eventhough the algebraic form of the convolution corresponding to these two problems is the same, the two problems are indeed very different. In the case of hierarchical models the distribution of the exchange interaction is studied, while in the problem we are discussing in this work one considers the distribution of the local field. This reflects the difference in the two underlying geometries. The d-dimensional hierarchical lattice include loops that are one of the essential characteristics that makes hierarchical lattices better candidates, within exactly solvable models, to study the problem of finite-dimensional SG [14]. The similarity between equations (15) and those related to hierarchical models is indicative of a deeper relation between the two (both geometries are hierarchical in the sense of ref. [43]) and will be the subject of future work.

C. The LDPC Phase Diagram - BSC

The calculated phase diagram for the Gallager LDPC code of rate $R = 1/4$ and a BSC of flip rate p as a function of the prior temperature $1/\beta F$ are shown if Fig. 1. We report both the location of the dynamical noise transition p_d, defined by the noise level at which suboptimal solutions emerge, and critical noise transition p_c, where the ferromagnetic solution ceases to be dominant, for all ranges of temperature $1/\beta F$. The phase diagram was calculated considering the flows of 10^3 quantities dictated by the convolution (12). As mentioned before the above number should be taken to the power $K-1$ to obtain the number of elementary operations within, e.g., the second equation of (14).

The location of the dynamical and critical transition values can be determined by analyzing the free-energy and the complexity as a function of the channel noise level for different values of the temperature $1/\beta$ (Fig. 2). We will refer noise level that corresponds to the emergence of sub-optimal solutions as the dynamical transition. At any value $p < p_d$, the computed free-energy (8) reduces to the ferromagnetic free-energy $f = -\frac{1-2p}{2}\log(\frac{1-p}{p})$. Consider first temperature values in the proximity of the Nishimori line. The trajectories exhibit a crossover to an unstable distribution first, and then flow to the ferromagnetic sink below $\simeq 0.1665$ (corresponding to a decoding success) or to a stable non-ferromagnetic distribution (corresponding to a decoding failure) above it. A similar behavior is observed for any temperature above the Nishimori line, the stable distribution being different for each values of the temperature $\beta < 1$. Rather different behavior is observed below the Nishimori line, where the unstable distribution is a strong coupling distribution, meaning that the average local field strength increases but the rescaled distribution remains constant. Finally, the trajectory flows again, either to the ferromagnetic sink or to a fixed local field distribution, which is stable under iteration of the recursion (15).

The computed free-energy, according to the convolution (15), is higher than the ferromagnetic free-energy

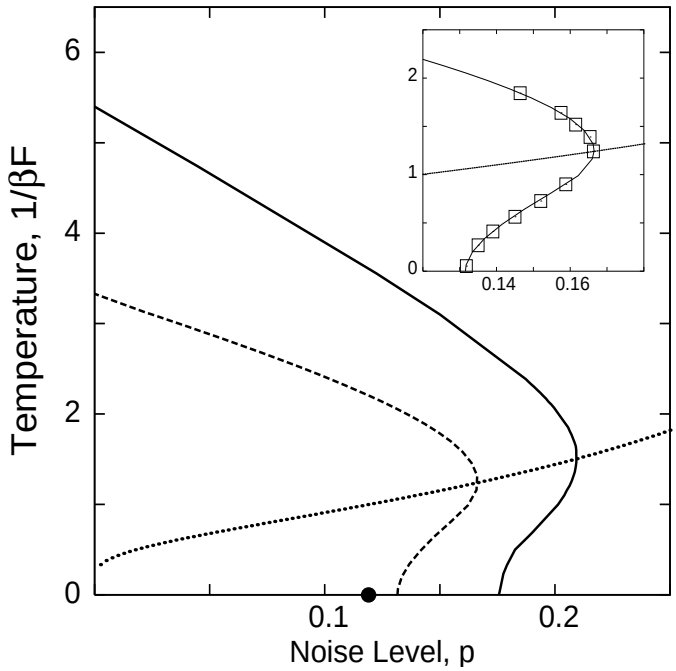

FIG. 1: The phase diagram for the LDPC code of rate $R = 1/4$ over the BSC channel. The solid and dashed lines represent the critical and dynamical transitions, respectively. The inset shows the curvature of the dynamical transition line boundary, together with decoding experiments results (square boxes). The dotted curve represents the Nishimori line. The black filled dot indicates the location of the dynamical transition at zero temperature assuming the local field distribution to be peaked over integer values only.

for all noise levels $p_d < p < p_c$. Above the critical noise value p_c, the computed free-energy becomes lower than the ferromagnetic free-energy. The location of the dynamical transition has been determined, at any temperature, considering the flows, under iteration, of the convolution (12), while the location of the critical noise threshold has been determined from the free-energy (8) as the point where the computed and the ferromagnetic free-energies coincides. In the inset of Fig. 1 we also report in square boxes the results of real decoding experiments obtained as follows. We iterated the probabilistic decoding algorithm [25], at different values of the noise channel p, for an ensemble of 10^3 networks of 10^4 and 2×10^4 nodes respectively. The inset shows the calculated mean values, the corresponding error being smaller than the corresponding symbol size. A precise estimate of the dynamical transition point has been obtained considering the percentage of decoding success within the network ensemble as a function of the noise level, for different system sizes, [44]. The decoding experiments were performed for different choices of the temperature. Along the Nishimori line (see Fig. 1) we find the value of $p_d \simeq 0.1665 \pm 0.0005$ in excellent agreement with the reported value for regular $R = 1/4$ Gallager codes [45].

Notice that the reentrant nature of both the dynamical and critical boundaries, as we found solving the convolution (14), is confirmed by the decoding experiments. In the range of noise levels $0.1315 < p < 0.1665$, decoding is possible only in a range of finite temperatures , as indicated in the inset of Fig. 1. The boundary between decodeable and undecodeable regions reaches its maximal value at the Nishimori temperature; zero temperature decoding fails at the same noise level. The reentrant nature of the critical phase boundary increases below the Nishimori line, but eventually weakens as the temperature is decreases further, a phenomenon that has already been discussed in a variety of different contexts [46, 47].

The fact that MPM and zero temperature BP/RS decoding do not coincide is not in contradiction with the results obtained in [48] which indicate that MAP and MPM decoding provide the same critical transition point. Clearly, zero temperature BP/RS decoding does not provide MAP results due to RSB effects. The latter and their effect on the phase diagram and on the reentrant nature of the phase boundaries will be further discussed in section IV.

An independent calculation has been performed at zero temperature. In this case the recursion relations (13) simplify and one finds limiting expressions for the two functions $u(\{x_i\}, J)$, $a(\{x_i\}, J)$. Implementing numerically such asymptotic expressions would require an independent calculation where one explicitly changes the recursion relations (13) to their asymptotic $\beta \to \infty$ form. The importance of the polynomials $R(\sigma)$ becomes clear at this point. At any temperature considered, we distinguish the finite and zero temperature contributions,

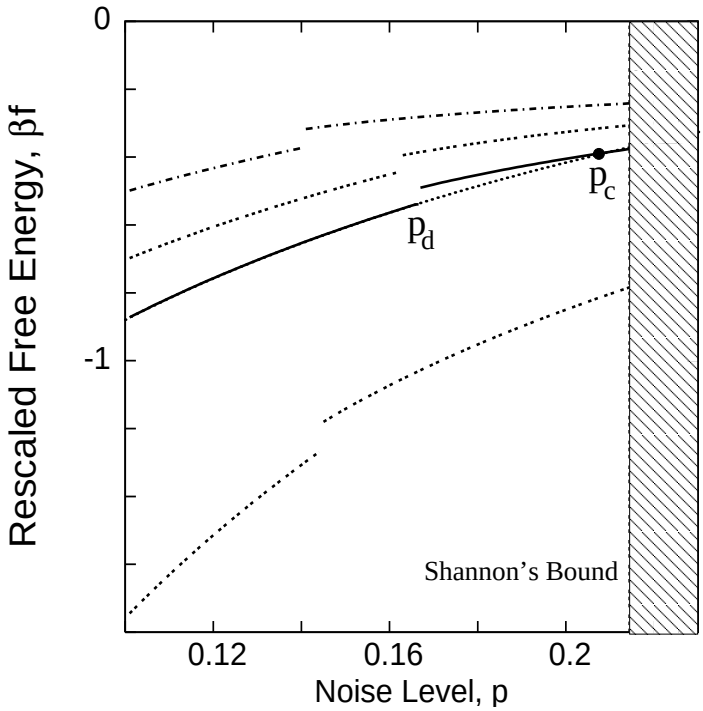

FIG. 2: The computed free-energy (8) as a function of the noise level p for different values of β. The solid line corresponds to the free-energy at the Nishimori line $\beta = 1$, while the dashed lines correspond to the values of $\beta = 8/6, 8/4$ below the Nishimori line and $\beta = 8/10, 8/14$ above it. For flip rates p larger than the dynamical transition the computed free-energy is higher than the ferromagnetic one, given by $f_{\rm Ferro} = -\frac{1-2p}{2} log(\frac{1-p}{p})$ (dotted-line).

corresponding to factorize the largest exponent in the sum (11), so that the limit of zero temperature is particularly simple to handle in our approach and no explicit changes are required in the recursion relations (13). We observe that at zero temperature the local field distribution is not peaked on integers as one might expect. We find that the relative weight of the background behind the integer-peaked distribution weakens as one consider the RSB solution, but restricting the distribution of the local fields to integer values, which results in a modification of the recursion relations (13) leads to different results. For LDPC (RS) decoding in the BSC this leads to an erroneous dynamical transition value of $p_d \simeq 0.121$, marked in Fig. 1 by a black filled dot, well below the reported zero temperature value of $p_d \simeq 0.1315$. Similar behavior occurs in the binary erasure channel problem if one simply neglects the background distribution, as we will discuss in section IV.

The initial condition $\pi^0(x) = (1-q)\delta(x-1)+q\delta(x+1)$, at $q = \frac{1}{2}$, has been used as initial condition for the BSC analysis. A dependence of the solution of the convolution (15) on the initial condition for the local field has been observed. We have studied the above convolution (15) for different choices of the initial condition in the form

$$\pi(x) = (1-q)\ \delta(x-1) + q\ \delta(x+1). \qquad (16)$$

The choice of $q = p$, where p is the flip rate of the channel results in the phase diagram of Fig. 3. *Any* choice of initial condition with $q > p$ (including the case $q = 1/2$ considered above) leads to the dynamical transition line (dashed line in Fig. 1), except for the choice $q = p$ which leads to a different dynamical transition. The location of the critical transition remains unchanged.

For instance, using the initial condition $q = p$, the dynamical transition along the Nishimori line is increased to $p_d \simeq 0.1734$, well above the known dynamical transition point. The physical interpretation of this behavior remains to be explained. Since it results from a simple change in the initial conditions of (12), one might argue that a properly modified decoding algorithm would enable us to decode above current p_d values; this is a possibility that we cannot rule out and further research is needed in order to elucidate this point.

We where able to perform a second set of decoding experiments that coincide with the dynamical transition line in Fig. 3 but only for noise level values below the value $p_d \simeq 0.1665$. The reentrant nature of the dynamical transition line (the dynamical transition at zero temperature being $p_d \simeq 0.158$) is reduced in this case.

D. Irregular Gallager Codes

For a constant K value one can select non-integer connectivity values of average $\bar{C}$ and consider a modified form of the convolution (15) that involves a linear com-

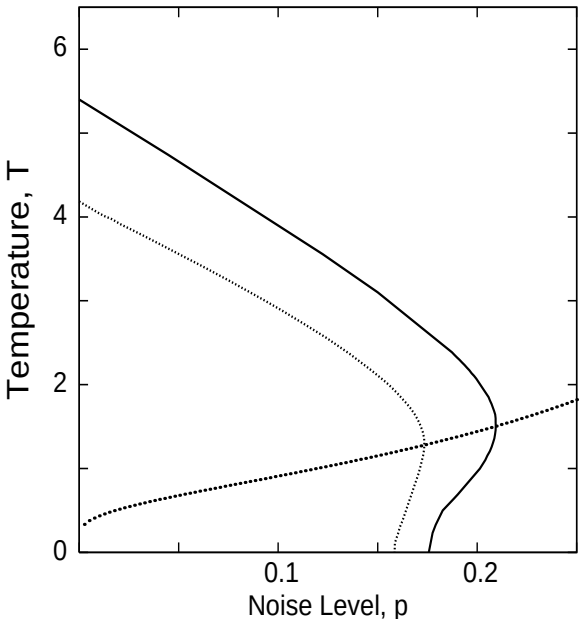

FIG. 3: The phase diagram of LDPC decoding for the BSC with the initial condition (16). The location of the critical transition in unchanged unlike the location of the dynamical transition, that has been observed to increase. We observe, on the Nishimori line, a dynamical transition occurring at $p_d \simeq 0.1734$, well above the ordinary dynamical transition of the regular Gallager code of rate $R = 1/4$.

bination of terms corresponding to different connectivity values. Non-integer values of the multi-spin interaction parameter K can also be easily accommodated in (15).

It has been reported that irregular low-density parity-check codes outperform regular constructions [25, 44].

We considered a generalized form of the convolution (15), (an explicit form is not provided for brevity) where both connectivity C and multi-spin interaction K take non-integer values such that the rate $R = 1-\bar{C}/\bar{K} = 1/4$ is preserved. In Fig. 4 we report the dynamical transition line for the regular construction $C = 3, K = 4$ ($R = 1/4$) already considered in the previous section together with the dynamical transition lines for irregular constructions of two values $K = 4$ and $K = 3$ and $C = 2$ and $C = 3$, such that $\bar{C} = 2.9, 2.8, 2.7$ (left to right) and $\bar{K} \simeq 3.87, 3.74, 3.6$. The dynamical transition value is observed to increase for the irregular constructions. This does not give a direct information on the specific pattern of irregularity that one should consider but provides quantitative information on the average connectivity/multi-spin interaction values one should investigate further. As for the regular case discussed earlier, a phase diagrammatic approach to the problem of irregular LDPC codes is important to understand the reason behind the successful decoding properties of irregular LDPC codes. A similar behavior to the one shown in Fig. 4, but less pronounced, has also been observed for LDPC decoding with the initial conditions (16) when $q = p$.

E. Finite connectivity problem with $C/K > 1$

We considered the finite-connectivity model (4) for the values of the connectivity $C = 9$ and $K = 4$. Despite the fact that it does not correspond to any Gallager LDPC code construction it is interesting to consider these connectivity parameters for two reasons: 1) They can represent code constructions in other variants of the LDPC family such as Sourlas or MN codes [25], and as such may also be linked to other LDPC-based applications. 2) They give rise to a SG behavior which is of interest. In Fig. 5 we report the corresponding phase diagram obtained considering the convolution (15). An SG phase occurs in this case. At low values of the flip rate p the convolution (12) flows to the ferromagnetic sink. In the vicinity of the dynamical transition line (marked in Fig 5 as the solid black line) the trajectories under iteration of the above convolution cross over to an unstable distribution and then either flow to the ferromagnetic sink, below the dynamical transition, or to a stable non-ferromagnetic distribution. For temperatures below the Nishimori line, at high enough values of the flip rate, the convolution instead flows to a spin-glass distribution.

IV. REPLICA SYMMETRY BREAKING

The role of RSB for the problem (4) is the subject of this and the following sections. The one-step RSB solution for the Bethe SG, as a special limiting case of

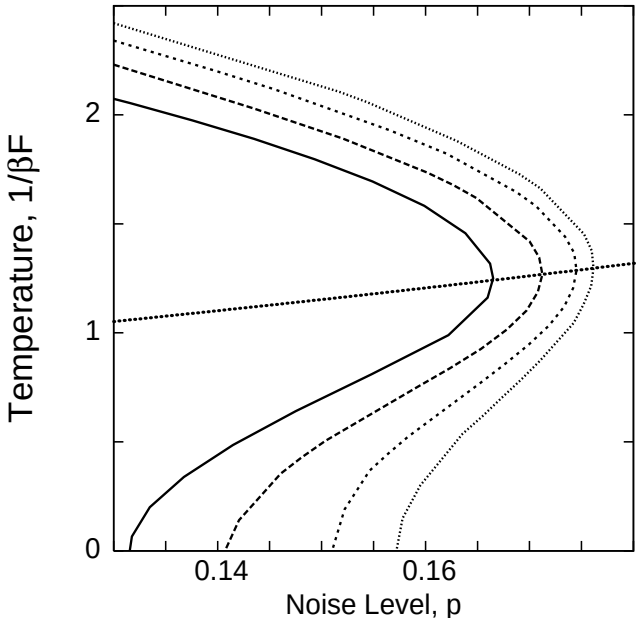

FIG. 4: Irregular LDPC phase diagram for the code rate R=1/4 . We show the dynamical transition for different values of the connectivity parameters C and K. The solid line corresponds to the dynamical transition line of a regular construction with $C = 3$ and $K = 4$. The dashed, dotted and thin-dotted lines correspond respectively to $\bar{C} = 2.9, 2.8, 2.7$, at constant rate $R = 1/4$. At lower average connectivity values, e.g. along the Nishimori line, the convolution (15) no longer flows to a ferromagnetic sink, but we observe a stable crossover to a distribution with large but finite average, so that successful decoding cannot be expected.

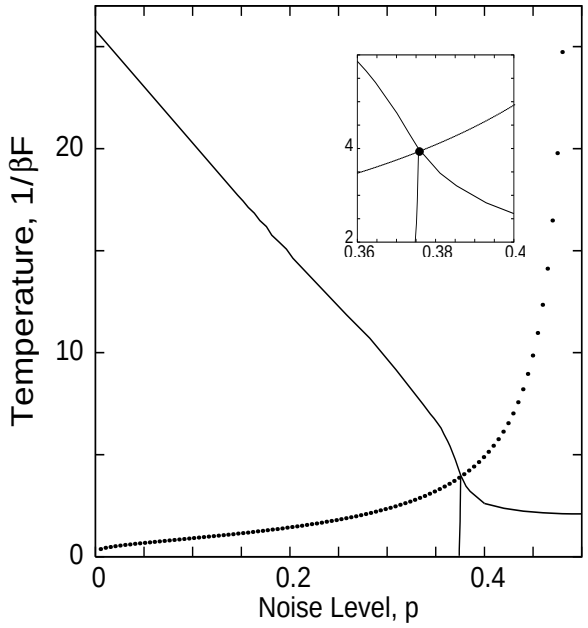

FIG. 5: The dynamical transition line for the finite-connectivity system with $C = 9$, $K = 4$. We report the location of the dynamical transition, shown now in thick solid lines. At high enough values of the flip rate, the convolution (15) either flows to a stable, asymmetric local field distribution (at high enough temperatures), or to a symmetric SG one (below the Nishimori line). Before flowing to the corresponding sink, the flows of the convolution (15) crosses over in the vicinity of either an unstable distribution above the Nishimori line, shown as the dotted line, or in the vicinity of a strong coupling unstable local field distribution below the Nishimori line. Similar behavior has been observed for the LDPC convolution (15) with the ordinary initial condition $q = 1/2$. In that case the location of the dynamical transition occurs at lower values of the noise channel probability. The inset shows the location of the dynamical boundaries together with the Nishimori line.

the Hamiltonian (4), has been studied in detail long ago. In this case it is well known that the RS solution is incorrect [11]. Recently, the onset of RSB phenomena in some limiting cases of the problem (4) has been considered, relying on the variational approximation [9] (for a recent formulation see [49]). Consider the equation for the global order parameter $g(\{\sigma^\alpha\})$, firstly introduced for the Bethe SG by Mottishaw, [5] in the general case of a multi-spin interaction parameter K,

$$g(\{\sigma_o^\alpha\}) = E_{J,\zeta}\big[Tr_{\{\sigma_i^\alpha\}} g^{C-1}(\{\sigma_1^\alpha\})\cdots g^{C-1}(\{\sigma_{K-1}^\alpha\}) \times \exp[\beta J\sum_\alpha \sigma_o^\alpha\sigma_1^\alpha\cdots\sigma_{K-1}^\alpha + \beta F\sum_{j\alpha}\sigma_j^\alpha]\big]. \tag{17}$$

where $\alpha = 1,\ldots,n$ labels different replicas of the system. The above expression holds in general, whether replica symmetry is broken or not (see Appendix B for the derivation). In the RS approximation one assumes that different replicas are equivalent and the functional order parameter $g(\{\sigma^\alpha\})$ depends only on the variable $\sigma = \sum_\alpha \sigma^\alpha$. In the limit of $n \to 0$, can be shown to satisfy,

$$g(\sigma) = E_{J,\zeta}\int\prod_{j=1}^{K-1}\frac{ds_j}{2\pi}g^{C-1}(is_j)\; du_j\; e^{iu_j s_j}\times \exp[-\sigma/\beta\tanh^{-1}(\tanh(\beta J)\prod_{j=1}^{K-1}\tanh(\beta u_j - F\zeta))]. \tag{18}$$

This equation corresponds to the equation that have been written for the Bethe SG, as soon as $K = 2$ and for vanishing message prior temperature $F = 0$ [5]. A derivation of equation (18) is found in Appendix B, where we show the equivalence of the above expression with the set of recursion relations (12), for the local field and conjugate distributions. In the one-step RSB approximation one assumes instead that the functional order parameter $g(\{\sigma^\alpha\})$ depends only on the variables $\sigma_M = \sum_\gamma \sigma_{M_\gamma}$, where $\alpha = (M,\gamma)$ is the replica index, $M = 1,\ldots,n/m$ and $\gamma = 1,\ldots,m$. In this case one finds that the corresponding equation for the functional order parameter $g(\{\sigma^\alpha\})$ becomes

$$g(\{\sigma_M\}) = \mathcal{N}^{-1}E_{J,\zeta}\int\prod_{j=1}^{K-1}\prod_{M=1}^{n/m}\frac{ds_{Mj}}{2\pi}g^{C-1}(is_{Mj}) \int\prod_{Mj}dr_{Mj}e^{ir_{Mj}s_{Mj}}\exp\Big[-\sum_M\sigma_M u(\{r_{Mj}\},J)\Big]\times \exp\Big[\frac{m}{2}\sum_M a(\{r_{Mj}\},J)\Big],$$

where the normalization is given by

$$\mathcal{N} = \int\prod_{j=1}^{K-1}\prod_{M=1}^{n/m}\frac{ds_{Mj}}{2\pi}g^{C-1}(is_{Mj}) \int\prod_{Mj}dr_{Mj}e^{ir_{Mj}s_{Mj}}\prod_j\cosh^m(\beta r_{Mj}). \tag{19}$$

The corresponding one-step RSB convolution follows, assuming that the order parameter factorize according to

$$g(\{\sigma_M\}) = \prod_{M=1}^{n/m} f(\sigma_M). \tag{20}$$

The assumptions behind the *factorized* ansätz (20), where the local field distribution is independent from the intra-group index, are discussed in [10]. In this case the one-step RSB convolution (19) become

$$\begin{aligned}\pi(x) &= E_\zeta\int\prod_{i=1}^{C-1}d\hat{x}_i\hat{\pi}(\hat{x})\delta\Big(x - \sum_{i=1}^{C-1}\hat{x}_i - F\zeta\Big)\\ \hat{\pi}(\hat{x}) &= \mathcal{N}^{-1}E_J\int\prod_{j=1}^{K-1}dx_j\pi(x_j)\exp[\mu a(\{x_j\},J)]\times \delta\Big(\hat{x} - u(\{x_j\},J)\Big),\end{aligned} \tag{21}$$

where the normalization $\mathcal{N}$ is given by

$$\mathcal{N} = \int\prod_{j=1}^{K-1}dx_j\pi(x_j)\exp[\mu a(\{x_j\},J)], \tag{22}$$

and where $\mu = m/\beta$. The above equations are valid, under the assumption (20), at finite temperatures and arbitrary connectivity values C and K. After its very first formulation [10] the convolution (21) has been studied in a range of different contexts, from random K-SAT to the coloring problem [50]. Using the identity,

$$\exp[\mu a(\{x_j\},J)] = \Big[\frac{2\cosh(u(\{x_j\},J))}{\prod_j\cosh(\beta x_j)}\Big]^\mu, \tag{23}$$

and substituting it in equation (21) one recovers the one-step RSB equations that have been also derived using the variational approach [5, 29, 49]. This shows that the so called frozen variational ansätz, considered in [9] and the factorized ansätz of [10] are equivalent. Even though there exists some degree of arbitrariness [51] in the way one redistributes the re-weighting between the two equations (21), we prefer the notation that involves the exponential of the energy term $a(\{x_j\})$, rather than the less obvious (and numerically more difficult to implement) parallel expression that follows considering the right hand side of (23) [49, 50]. The simplified expression of the free-energy presented in section III was obtained in virtue of the same identity (23), and the same degree of freedom writing the free-energy was already discussed for the Bethe SG [11] (the right hand side of (23) being, at $K = 2$ the function $c(x,J)$ discussed in ref. [11]).

A. The Bethe SG

We apply the method described in section III to study the one-step RSB convolution (21) of the Bethe SG, which has been extensively studied and recently considered also in its ferromagnetically biased version [15]. In this case the distribution of the quenched random variable J is

$$P(J) = \frac{1+\rho}{2}\delta(J-1) + \frac{1-\rho}{2}\delta(J+1), \qquad (24)$$

and where the parameter $\rho \in [0,1]$ is $\rho = 1$ for a ferromagnet and $\rho = 0$ for the unbiased Bethe SG. The Bethe SG corresponds indeed to the original problem (1) at $K = 2$. We will present results obtained at zero temperature. In the zero temperature limit we find the following expression for the free energy $\Phi(\mu)$,

$$\Phi(\mu) = \Delta E^{(1)} - \frac{C}{2}\Delta E^{(2)}, \qquad (25)$$

where explicit expressions for the site and link contributions to the ground state energy are

$$\begin{aligned}
\exp\left(-\mu\Delta E^{(1)}\right) &= \int \prod_{j=1}^{C} dx_j \pi(x_j) \times \\
&\exp\left(\mu \sum_{j=1}^{C} a(\{x_j\}, J_j) + \mu| \sum_{j=1}^{C} u(\{x_j\}, J_j)|\right) \\
\exp\left(-\mu\Delta E^{(2)}\right) &= \int \prod_{j=1}^{2} dx_j \pi(x_j) \times \\
&\exp\left(\mu \max_{\sigma_1,\sigma_2}(x_1\sigma_1 + x_2\sigma_2 + J\sigma_1\sigma_2)\right),
\end{aligned} \qquad (26)$$

corresponding, at $\mu = 0$ and $K = 2$, to the RS equation (8) in the zero temperature limit and neglecting the prior term in (4). Similar expression have been discussed in [11]. In the limit of zero temperature one finds $a(J,x) = |x| + \delta_{x,0}$ and $u(x,J) = JS(x)$, being $S(x=0) = 0$, and $S(x \neq 0) = sgn(x)$. In what follows we present results obtained under the *integer peaked* ansätz as well as for the full distribution. The relative importance of non-integer values in the distribution that solves the above convolution (21) is rather limited in this case. The background behind the integer peaked values weakens as one consider the one-step RSB case, and may disappear in a fully replica symmetry broken scenario [11]. In Fig. 6 we show the ground state energy as a function of the replica symmetry breaking parameter μ for different values of the ferromagnetic bias using the integer peaked ansätz and in the case of the full local field distribution. The ground state energy one extrapolates including the background calculation is higher than the one obtained within the three peak ansätz [10]. In Fig. 7 we show the corresponding complexity or configurational entropy, that can be obtained as a parametric plot in terms of the RSB parameter μ, the free-energy $f(\mu)$ being its Legendre transform [4]. We observe a positive complexity for all reported values of ρ. At higher values of the ferromagnetic bias $\rho > \rho^* \simeq 0.74$ a positive complexity is not observed anymore. One should also consider that the above values should be extrapolated in the limit of large number of bins, so that one expects a slightly higher value $\rho^* \simeq 0.75$. In Fig. 8 we show the magnetization for in the replica symmetric and one-step replica symmetry broken solution at different values of the ferromagnetic bias. At values $\rho < 0.65$ one recovers the results known for the unbiased Bethe SG. The solid line indicates the magnetization computed in the replica symmetric approximation (notice that this is a computed magnetization for a finite number of bins, so that it approaches the expected value of $\rho_{RS} = 0.75$ from below), while the square boxes represent the magnetization in the one step RSB approximation without considering the background. For each value of ρ, we extrapolated the magnetization that corresponds to the value of μ where the ground state energy has a maximum. Similarly, the dashed line points to the results obtained considering the true convolution (12), that includes non integer values of the local field. The putative size of the so called *mixed phase*, previously discussed [15], if any, is rather small and do not agree with previous estimates (we observe the magnetization within the RSB calculation to vanish at values of $\rho \simeq 0.75$, if one considers a large enough number of bins within the calculation, implying that the size of the mixed phase, if any, is vanishingly small). It should be said however that the calculation of [15] considered a full one step RSB calculation, in the sense of [11], where the factorized approximation is relaxed. To investigate this point better, we performed the following: instead of implementing the convolution (12) within the factorized approximation [10], we choose a population of 5×10^5 distributions (including a site dependence). At each step of the iteration process we consider pairwise-convolutions of local field distributions corresponding to different sites, selected at random; after a transient regime, we obtain the equilibrium population. Waiting a number of iteration steps of the order of the population size, according to our calculation, the local field distributions become site independent, meaning that the factorized approximation provides similar results to those of the full RSB ansätz. If one compares Fig. 7 with the corresponding plot in ref. [15], where a similar calculation of the complexity is presented, we see that the location of the maximum of the complexity as a function of μ *decreases* for increasing ρ values (see Fig. 7), as one might intuitively expect, increasing the ferromagnetic bias.

B. The Binary Erasure Channel

In the case of the BEC discussed in section II, the form of the convolution (15) simplifies and the distribution of the local field, and its conjugated distribution become bi-

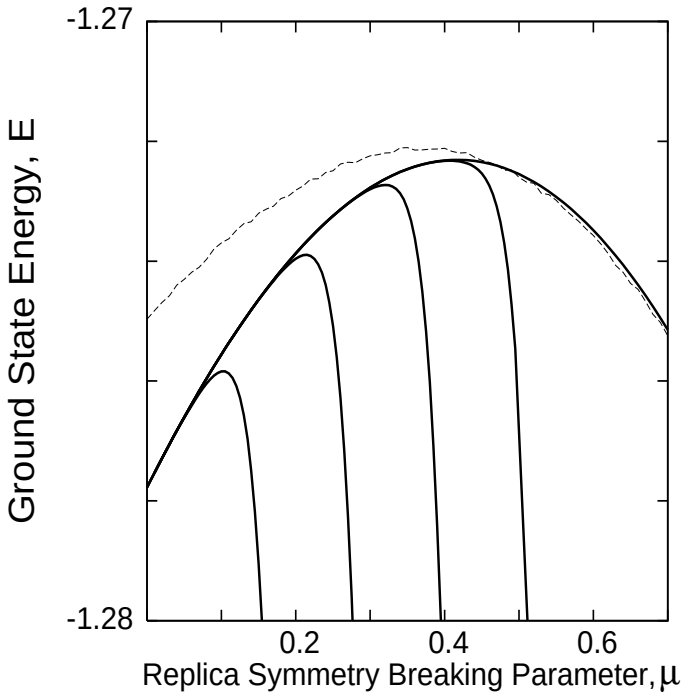

FIG. 6: The ground state energy as a function of the replica symmetry breaking parameter for different values (from left to right) of the bias $\rho = 0.66, 0.68, 0.70, 0.72, 0.74$. We also show in thin dotted line the ground state energy including the background distribution as in ref.[3].

modal. Despite its simplicity the binary erasure channel problem is of practical relevance [52, 53]. For the BEC one writes the convolution (15) as

$$\begin{aligned} \pi(x) &= \rho\delta(x) + (1-\rho)\delta_\infty(x) \\ \hat{\pi}(\hat{x}) &= \hat{\rho}\delta(\hat{x}) + (1-\hat{\rho})\delta_\infty(\hat{x}) \end{aligned} \tag{27}$$

where $\delta_\infty(\cdot)$ is a delta function located at $+\infty$, $\rho(x)$ is the distribution of the effective local field and $\hat{\rho}(\hat{x})$ its conjugate distribution. The resulting convolution [29] involving the two distributions $\rho(x)$ and $\hat{\rho}(\hat{x})$, in the one-step RSB case, is given by

$$\begin{aligned} \rho(x) &= \int \prod_{l=1}^{C-1} d\hat{x}\ \hat{\rho}(\hat{x})\ \delta\Big(x - \sum_{l=1}^{C-1} \hat{x}_l\Big), \\ \hat{\rho}(\hat{x}) &= \sum_{\nu}^{K-1} f_\nu \mathcal{N}_\nu \int \prod_{i=1}^{\nu} dx_i\ \rho(x_i)\ \exp[\mu a(\{x_i\}, J)] \times \\ &\quad \delta\big(\hat{x} - u(\{x_i\}, J)\big), \end{aligned} \tag{28}$$

where f_ν are the binomial coefficients of order $K-1$ and $\mathcal{N}_\nu$ the set of normalization coefficients defined by

$$\mathcal{N}_\nu = \int \prod_{i=1}^{\nu} dx_i \rho(x_i) \exp[\mu a(\{x_i\}, J)]. \tag{29}$$

One can readily check that the above convolution reduces to the variational approximation [9, 29] using identity (23). We note that the variational ansätz, as already discussed for the case of the BSC, coincides with the factorized ansätz (20) [5, 10]. We consider an explicit expression for the one step RSB free-energy that involves the binomial coefficients of order K. Within the factorized hypothesis [10], the expression for the free-energy is easily computed as a function of the RSB parameter μ. We present results for the BEC at zero temperature for values of the code rate R=1/4 and $R = 1/2$ (note that we also consider in what follows the integer peak ansätz for the local field distribution [29] in order to compare with the general case of non-integer local fields). In the inset of Fig. 9 we show the energy as a function of the erasure probability p for the rate value $R = 1/2$ within the integer valued local field approximation. Notice that the integer value approximation corresponds to having only three bins in our approach of section III. In Fig. 10 we compare the results within and without the integer approximation for a code rate $R = 1/4$. The dynamical transition is defined as the point where sub-optimal solutions emerge the corresponding complexity being non zero, as already discussed for the BSC channel (see Fig. 10). The location of the dynamical transition is also the point where the recursion (21) flows to a subdominant distribution, rather than the ferromagnetic sink. This coincides with the point where algorithms devised for real decoding experiments fail to decode the original message. Within the RS framework, we find that the location of the dynamical transition changes significantly if non-integer values

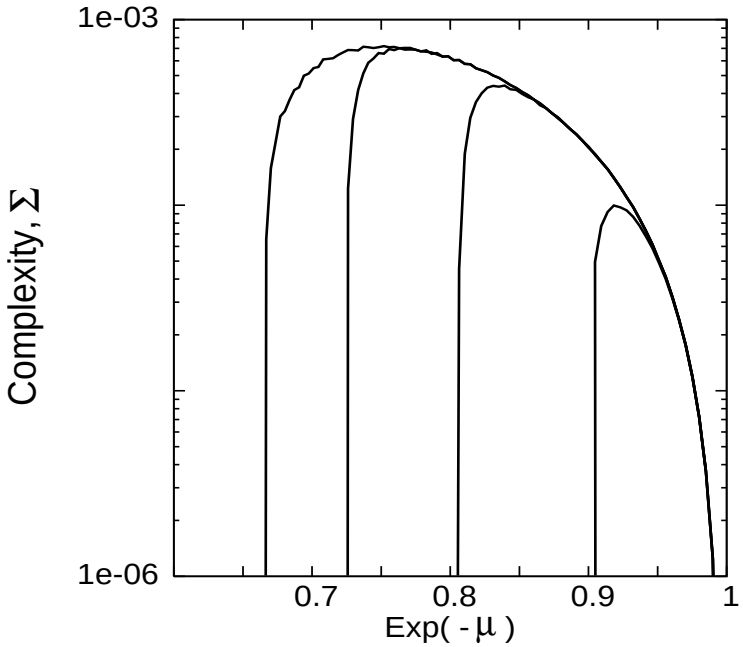

FIG. 7: The complexity Σ as a function of $\exp(-\mu)$ for different values of the ferromagnetic bias $\rho = 0.66, 0.68, 0.70, 0.72, 0.74$, within the three peak ansätz.

of the local field are taken into account. Within the three peak ansätz the local field distribution is simply defined as [21]

$$\rho(x) = \rho_+ \delta(x-1) + \rho_- \delta(x+1) + \rho_0 \delta(x) \qquad (30)$$

The calculation we performed within the integer local field approximation (for rates $R = 1/2$ and $R = 1/4$ in Fig. 9 and Fig. 10 respectively) might suggest to interpret the point $p^* \simeq 0.4294$ for the rate value $R = 1/2$ as the dynamical transition point [29]. If however one compares (see Fig. 10) with the results of the local field distribution that now includes non-integer values (the thick solid line corresponding to $\rho_{x>0}$) we see that the location of the dynamical transition is rather different. Moreover the behavior of the local field probability $\rho_\pm$ around the value $p^* \simeq 0.4294$, within the *three peak* ansätz is rather suspicious. Indeed, including non-integer values of the local field turns out to be crucial for having a quantitative description of the dynamical transition and possibly explains the disagreement with numerical experiments that has been reported lately for the R=1/2 BEC problem [29]. If one avoids the *three peak* ansätz, the nature of the flows dictated by the recursion (28) is smooth as it always leads to a well-behaved behavior of the probability densities $\rho_{x>0}$ and $\rho_{x<0}$. Up to this point all considerations are still within the RS approximation.

Moreover, considering the full convolution (28) as we do in what follows, the location of the dynamical transition in the one-step RSB solution becomes higher than that obtained within RS, which arguably implies that one may be able to construct the algorithmic analog of the RSB recursion (28) to improve decoding performances. Similarly, within the RSB calculation, the location of the critical transition is increased for the rate $R = 1/4$ considered above and found to be very close to the Shannon bound value $1 - R = 0.75$ (cfr. Fig. 13).

We iterated the convolution (28) within the one-step RSB approximation described in section VI and computed the free-energy as a function of the RSB parameter μ for several values of the erasure probability p, above the dynamical transition point $p_d \simeq 0.602$ as reported in Fig. 11. In this range of p values, the free-energy grows as a function of μ, dropping to the ferromagnetic free-energy value (being $f_{\text{Ferro}} = 0$ for the BEC) at some critical μ^*. At higher values of the erasure probability p, the free-energy eventually drops to zero after having reached its maximum (see Fig. 11). According to the standard recipe of maximizing the free-energy with respect to μ [33], we extrapolate the value of the dynamical transition within the one-step RSB calculation, finding the value of $p_d^{RSB} \simeq 0.621$, indicated in Fig. 10 by the dotted line, well above the RS value $p_d^{RS} \simeq 0.602$. The corresponding complexity is shown in Fig. 12, for different values of the erasure probability considered. We observe two branches, a physical (right) and an unphysical one (left) as explained in ref. [11]. From the former branch we extrapolated the RSB energy value corresponding to the noise channel probability. Notice that above the RS dynamical transition we do observe, for values of $p \simeq 0.606, 0.613, 0.62$ that the second branch, that is the relevant one, is not present. This can be explained because the corresponding curves for the free-energy (Fig. 11) do not reach a maximum and drop instead to the ferromagnetic energy value ($f = 0$). The dynamical transition within the RSB

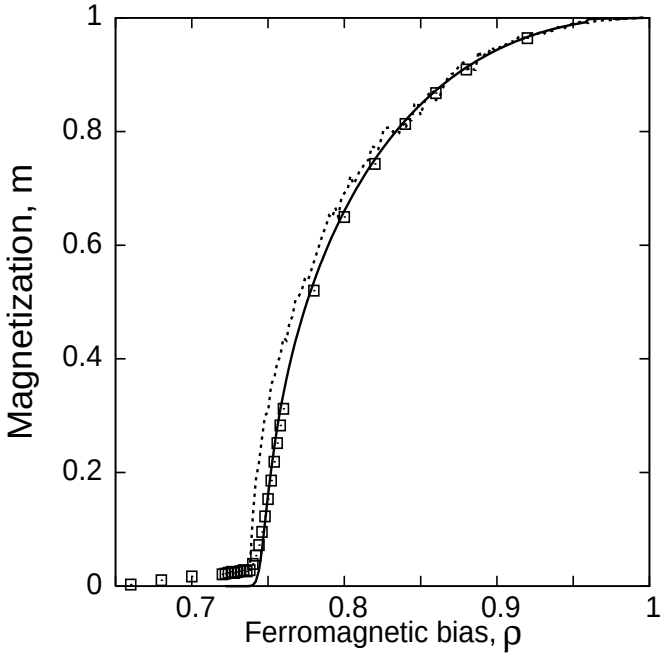

FIG. 8: The magnetization as a function of the ferromagnetic bias ρ. The thick solid line correspond to the RS calculation obtained with 4096×4 bins. Square boxes correspond to the one step RSB calculation if one neglects the background local field distribution. Finally the dotted line represents the one step RSB calculation including the background calculation, according to equation (21) and was obtained with 32768×4 bins.

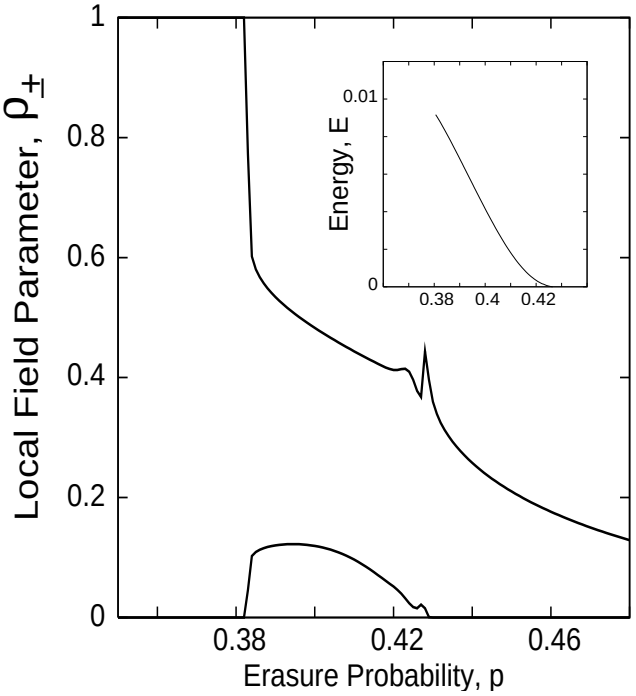

FIG. 9: For the code rate R=1/2 and a BEC channel we report the local field parameter $\rho_{\pm}$ as a function of the erasure probability p, at zero temperature, within the integer value ansätz (30). The continuous lines represent respectively the probability of a negative ρ_{-} and positive ρ_{+} local field. The inset shows the computed energy as a function of the erasure probability.

calculation increases.

If one considers the free-energy as a function of the RSB parameter μ at values of the erasure probability slightly higher that the RS critical transition point, one finds that the maximum is located at positive energies, implying that the critical transition point also changes under the one step RSB calculation. In this way (Fig. 13) we extrapolated the value of the critical transition, within the RSB approximation, to $p_c^{RSB} \simeq 0.7450 \pm 0.05$. Note that Shannon's bound for the specific code rate considered is $1 - R = 3/4$. In comparison, the critical RS transition point $p_c^{RS} \simeq 0.6695$. The fact that the dynamical and critical transition points increase within the one-step RSB calculation might be surprising at first. In the next section we will show that a similar situation is observed for the BSC at temperatures below the Nishimori condition [26], where it is known that the RS solution is dominant [54]. It is also reasonable to believe that the above one step RSB calculation is exact for this problem [11] [50]. The above findings concerning the location of the critical (RSB) transition seem to support this belief.

C. The Binary Symmetric Channel

In this section we return to the BSC (4) and employ the same considerations discussed for the BEC in the previous section. We consider the convolution (21) along the Nishimori line $\beta = 1$. The location of the dynamical transition has been discussed in section III and we found the value of $p_d^{RS} = 0.1665$ within the RS approximation, in agreement with probabilistic decoding estimates. Not surprisingly [54], if one looks at the free-energy as a function of the RSB parameter μ for values of the BSC noise probability $p > p_d$, one finds that the free-energy decreases (see the inset in Fig. 14), indicating that the RS solution is dominant, so that the dynamical transition is the same in the one-step RSB case. $p_d^{RS} = p_d^{1RSB}$. However, at temperatures well below the Nishimori line instead, i.e. $\beta = 8.0$, we observe the following facts: above the RS dynamical transition $p_d^{RS} \simeq 0.135$ the free-energy increases as a function of the RSB parameter μ, dropping to the corresponding ferromagnetic free-energy at some value μ^*, before reaching a maximum. This means that the second, physical branch of the complexity is not present, the analysis following the same lines as for the BEC calculation. At higher values of the flip rate, i.e. $p \simeq 0.18$ the second branch of the complexity (see Fig. 15) appears, indicating a non-zero complexity and that we are above the RSB dynamical transition. The corresponding complexity for the LDPC decoding at $p = 0.185$ is reported in Fig. 15. These findings imply that the location of the dynamical transition is improved with respect with the RS value.

The same behavior has been observed, progressively reducing in importance at higher values of the temperature $T = 2/8$ and $T = 4/8$, while at $T = 1$, corresponding to the Nishimori line, this phenomenon is no longer observed. The inset of Fig. 14 shows the computed free-energy as a function of the RSB parameter μ at the Nishimori temperature channel noise $p = 0.174$. We conclude observing that, below the Nishimori line, the reentrant nature of the dynamical transition is not observed within the RSB calculation.

V. CONCLUSIONS AND FUTURE PERSPECTIVES.

We introduced a new method to compute the phase diagram of finite-connectivity SG model systems and discussed the connection with LDPC codes. We extended the one-step RSB theory, originally formulated for the Bethe SG problem, to the Gallager LDPC decoding for two different type of corruption processes, BEC and BSC. For the BEC at zero temperature we found that the location of the dynamical transition increases with respect to the RS case. Our estimate for the RSB critical transition value is a mere one percent away from capacity, differently from the RS estimate. The critical and dynamical properties of LDPC decoding have also been studied for the case of a BSC. The reentrant nature of the LDPC phase diagram and the corresponding changes that RSB implies in its low temperature properties have also been studied. We found that below the Nishimori line the dynamical transition increases within the RSB theory. Possible implications to improve the decoding performances of the state-of-the-art error correcting codes are one of the perspectives we wish to address. We would like to construct the algorithmic analog of the convolution (21) in order to improve the decoding performances as predicted by the RSB theory. The method we used to determine the phase diagrams along this work is very promising. It allows to study, without loss of continuity, rather different problems, ranging from the d-dimensional hierarchical SG to finite-connectivity mean-field models. In this sense it would be very interesting to apply this method to clarify a few open issues. On the one side we would like to investigate, within the one-step RSB theory, the finite temperature phase diagram of the Bethe SG in a magnetic field. On the other, it would be interesting to explore the presence, if any, of RSB phenomena in d-dimensional SG hierarchical model systems.

Acknowledgments

This work was supported in part by the European Community's Human Potential Programme under contract number HPRN-CT-2002-00319.

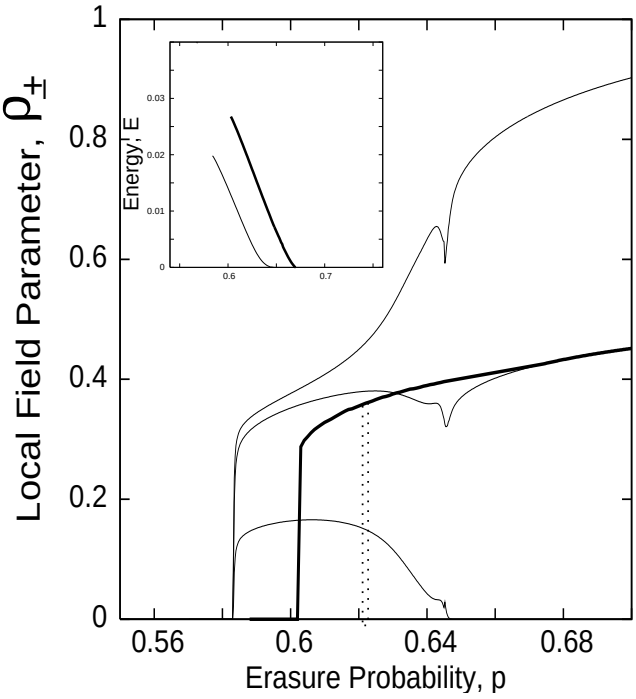

FIG. 10: For a code rate R=1/4 and a BEC channel at zero temperature, we report the local field parameters as a function of the erasure probability p, for the ansätz (30) shown in thin lines, corresponding to ρ_-, $\rho_- + \rho_0/2$ and ρ_0. We then report (thick line) the results for the local field probability according to the full convolution (28), as it is in the simplest RS approximation $\mu = 0$, corresponding to $\rho_{x<0}$, being $\rho_{x>0} = 1 - \rho_{x<0}$. The dashed vertical line corresponds instead to the location of the dynamical transition within the one step RSB calculation. The inset shows the computed energy as a function of the erasure probability. within the *three peak* ansätz (thin line) and in the case of the full convolution of the local field being considered (thick solid line).

[1] Y. Imry and S. Ma, Phys. Rev. Lett. **35**, 1399 (1975).
[2] S.F. Edwards and P.W. Anderson, J. Phys. F **5**, 965 (1975).
[3] K. Wong and D. Sherrington, J. Phys. A **20**, L785 (1987).
[4] M. Mézard and G. Parisi, Europhys. Lett. **3**, 1067 (1987).
[5] P. Mottishaw, Europhys. Lett. **4**, 333 (1987).
[6] C. DeDominicis and P. Mottishaw, J. Phys. A **20**, L375 (1987).
[7] C. DeDominicis and Y.Y. Goldschmidt, J. Phys. A **22**, 399 (1989); C. DeDominicis and Y.Y. Goldschmidt, Phys. Rev. B **41**, 2184 (1990).
[8] H. Rieger and S. Kirkpatrick, Phys. Rev. B **45**, 9772 (1992).
[9] R. Monasson, J. Phys. A **31**, 513 (1998).
[10] Y.Y. Goldschmidt and P.Y. Lai, J. Phys A **23**, L775 (1990).
[11] M. Mézard and G. Parisi, Eur. Phys. J. B **20**, 217 (2001); M. Mézard and G. Parisi, J. Stat. Phys. **111**, 1 (2003).
[12] M. Mézard, G. Parisi, and R. Zecchina, Science **297**, 812 (2002).
[13] R.C. Dewar and P. Mottishaw, J. Phys. A **21**, L1135 (1988).
[14] G. Migliorini and A.N. Berker, Phys. Rev. B **57**, 426 (1998).
[15] T. Castellani, F. Krzakala, and F. Ricci-Tersenghi, cond-mat 0403053.
[16] R.G. Gallager Low Density Parity Check Codes, IRE Trans. Inf. Theory **IT-8**, 21 (1962); R.G. Gallager, Low Density Parity Check Codes, Research Monograph Series **21**, Cambridge, MA: MIT Press (1963).
[17] C.E. Shannon, Mathematical Theory of Communication. Bell Sys. Tech. J. **27**, (pt I) 379, (pt II) 623 (1948).
[18] T. Cover and J. Thomas, Elements of Information Theory, New York: Wiley (1991).
[19] N. Sourlas, Nature **339**, 693 (1989).
[20] Y. Kabashima and D. Saad, Europhys. Lett. **45**, 97 (1999).
[21] R. Vicente, D. Saad, and Y. Kabashima, Phys. Rev. E **60**, 5352 (1999).
[22] A. Montanari, Eur. Phys. J. B, **23**, 121 (2001).
[23] B. Derrida, Phys. Rev. B **24**, 2613 (1981).
[24] K. Nakamura, Y. Kabashima and D. Saad, Europhys. Lett. **56**, 610-616, (2001).
[25] D.J.C. MacKay, IEEE Trans. Inf. Theory **45**, 399 (1999).
[26] H. Nishimori, J. Phys. C **13**, 4071 (1980).
[27] H. Nishimori, J. Phys. Soc. Japan **62**, 2973 (1993).
[28] Y. Iba, J. Phys. A **32**, 3875 (1999).
[29] S. Franz, M. Leone, A. Montanari, and F. Ricci-Tersenghi, Phys. Rev. E **66** 046120 (2002).

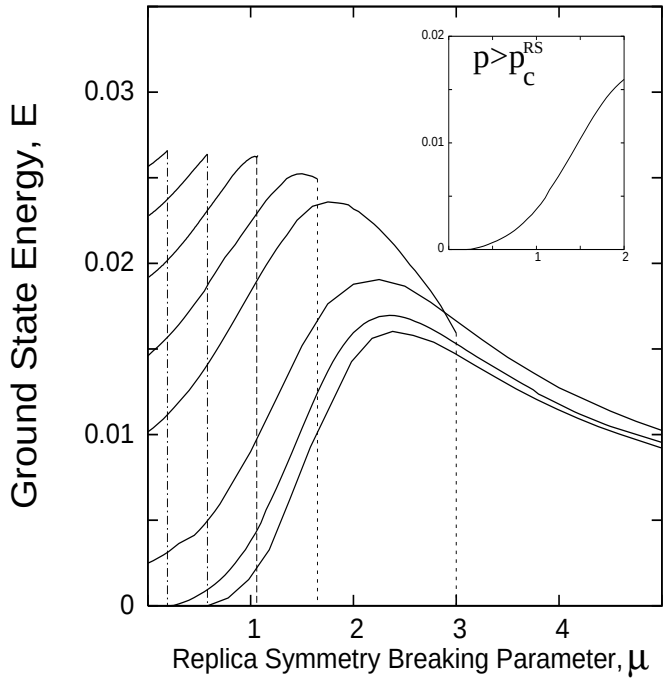

FIG. 11: The one step RSB free energy as a function of the parameter μ for different values (left to right) of the erasure probability $p = 0.606, 0.613, p = 0.62, 0.63, 0.64, 0.66$, and $p = 0.67$. The first two curves, corresponding to y $p = 0.606$, $p = 0.613$ drop to zero before a maximum is reached as a function of μ, indicating the absence of the physical branch of the complexity. Differently, around values of $p \simeq 0.625$ the energy reaches a maximum *before* dropping to zero, so that the physical branch of the complexity appears. The inset shows the ground state energy as a function of the RSB parameter μ, at a flip rate above the critical transition point.

[30] Y. Kabashima and D. Saad, J. Phys. A , R1 (2004).
[31] D. Bowman and K. Levin, Phys. Rev. B **25**, 3438 (1982).
[32] Y. Fu and P.W. Anderson, J. Phys. A **19**, 1605 (1986).
[33] M. Mézard, G. Parisi and M. Virasoro, Spin Glass Theory and Beyond, Singapore: World Scientific (1987).
[34] T.Murayama, Y. Kabashima, D.Saad and R. Vicente, Phys. Rev. E **62**, 1577 (2000).
[35] T. Tanaka and D. Saad, J. Phys. A **36**, 11143 (2003).
[36] F. Kschischang and B. Frey, IEEE J. Selected Areas Commun. **2**, 153 (1998).
[37] J. Pearl, Probabilistic Reasoning in Intelligent Systems, San Francisco, CA: Morgan Kaufmann Publishers Inc. (1988).
[38] J.S. Yedida, W.T. Freeman, and Y. Weiss, Advances in Neural Information Processing Systems **13**, T.K. Leen, T.G. Dietterich and V. Treps (eds.), Cambridge, MA: MIT Press (2001).
[39] M. Opper and D. Saad (editors), Advanced Mean Field Methods - Theory and Practice, Cambridge, MA: MIT press (2001).
[40] D. Andelman and A.N. Berker, Phys. Rev. B **29**, 2630 (1984).
[41] M. Hinczewski and A.N. Berker, cond-mat 0507293.
[42] A.N. Berker and S.R. MacKay, Phys. Rev. B **33**, 4712 (1986).
[43] M. Kaufman and B. Griffiths, Phys. Rev. B **24**, 496 (1981); B. Griffiths and M. Kaufman, Phys. Rev. B **26**, 5022 (1982).
[44] I. Kanter and D. Saad, J. Phys. A **33**, 1675 (2000).
[45] T. Richardson and R. Urbanke, IEEE Trans. Inf. Theory, **47**, 599 (2001).
[46] S.R MacKay, A.N. Berker, and S. Kirkpatrick, Phys. Rev. Lett. **48**, 767 (1982).
[47] C. Amoruso and A.K. Hartmann, cond-mat 0401464.
[48] J. van Mourik, D. Saad and Y. Kabashima, Phys. Rev. E **66**, 026705 (2002).
[49] Y. Kabashima, cond-mat 0506311.
[50] S. Franz, M. Leone, F. Ricci-Tersenghi, and R. Zecchina, Phys. Rev. Lett. **87**, 127 (2001).
[51] M. Mézard and R. Zecchina, Phys. Rev. E, **66**, 56126 (2002).
[52] M.G. Luby, M. Mitzenmacher, M.A. Shokrollahi, and D.A. Spielman, IEEE Trans. Inf. Theory **47**, 569 (2001).
[53] T. Richardson and R. Urbanke, Codes, Systems, and Graphical Models, B. Marcus and J. Rosenthal (eds.), New York, NY: Springer (2001).
[54] H. Nishimori and D. Sherrington, Disordered and Complex Systems, P. Sollich, A. Coolen, L. Hughston and R.Streater (eds.), New York, NY:AIP, 67 (2001); P. Le Doussal and A.B. Harris, Phys. Rev. Lett **61**, 625 (1988).

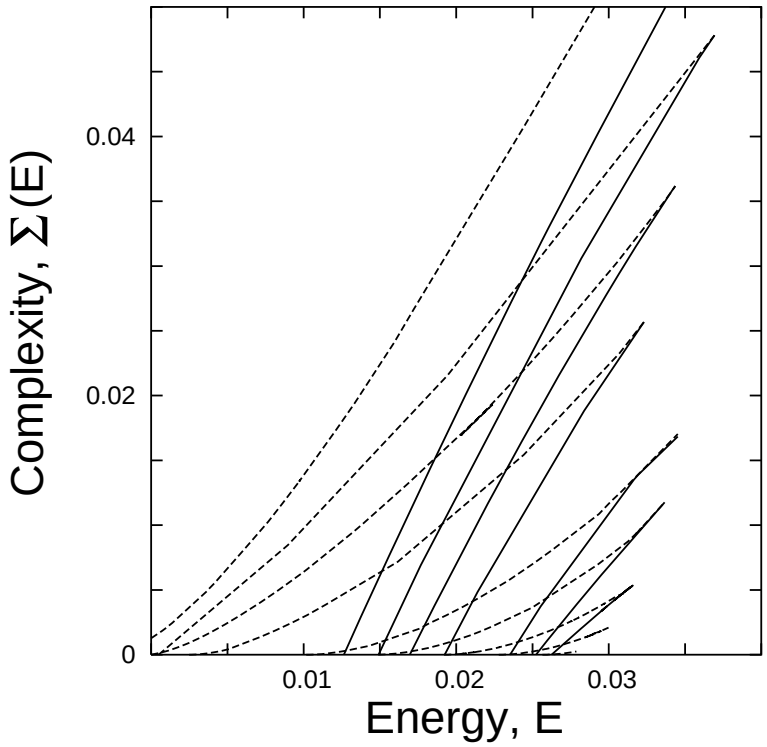

FIG. 12: Complexity $\Sigma(E)$ as a function of the Ground State Energy E for different values of the erasure probability p. From right to left $p = 0.606, 0.613, 0.62, 0.63, 0.64, 0.66, 0.67, 0.68$ and $p = 0.69$ for the code rate problem $R = 1/4$.

Appendix A - Equivalence of the RS Equations

Considering the replicated partition function,

$$\langle \mathcal{Z}^n \rangle_{\mathcal{A},\zeta,J} = E_{\mathcal{A},J,\zeta} Tr_{\{S_j^\alpha\}} \times e^{\beta F \sum_{\alpha,k} \zeta_k S_k^\alpha + \beta \sum_{\alpha,k} \mathcal{A}_\mu J_\mu S_{i_1}^\alpha \cdots S_{i_K}^\alpha} \tag{31}$$

one can perform the average over the corresponding underlying geometry in (31) introducing an integral representation for the finite-connectivity constrain $\delta(\sum_{\mu\setminus i} \mathcal{A}_\mu - C)$ in the spirit of [3], defining the set of overlaps $q_{\alpha_1 \cdots \alpha_m}$ and conjugated functional order parameter $\hat{q}_{\alpha_1 \cdots \alpha_m}$, [20]. This leads, under the RS ansätz,

$$\begin{aligned} q_{\alpha_1 \cdots \alpha_m} &= \int dx\ \pi(x) x^m \\ \hat{q}_{\alpha_1 \cdots \alpha_m} &= \int d\hat{x}\ \hat{\pi}(\hat{x}) \hat{x}^m, \end{aligned} \tag{32}$$

to the following expression for the free energy,

$$\begin{aligned} \beta f = &- \frac{C}{K} \ln \cosh \beta J - \frac{C}{K} E_J \int \Big[\prod_{l=1}^{K} dx_l \pi(x_l) \Big] \\ &\times \ \ln \Big[1 + \tanh(\beta J) \prod_{j=1}^{K} \tanh(\beta x_j) \Big] \\ &+ \ C \int dx d\hat{x} \pi(x) \hat{\pi}(\hat{x}) \log \big(1 + \tanh(\beta x) \tanh(\beta \hat{x}) \big) \\ &+ \ C \int dy \hat{\pi}(\hat{x}) \log \cosh(\beta \hat{x}) \\ &- \ E_\zeta \int \prod_{l=1}^{C} dy_l \hat{\pi}(x_l) \Big[2 \cosh \beta (\sum_{l=1}^{C} \hat{x}_l + F\zeta) \Big]. \end{aligned} \tag{33}$$

The corresponding saddle point equations (14) are derived differentiating the above expression with respect to the local field $\pi(x)$ and its conjugated distribution $\hat{\pi}(\hat{x})$. In order to obtain the free-energy (8), the second and third term in (33) can be combined via equation (14), to obtain

$$\begin{aligned} II + III \equiv &+ \ C \frac{K-1}{K} \Delta f^{(2)} - C \frac{K-1}{K} \log \cosh \beta J \\ &- \ C(K-1) \int dx\ \pi(x) \log \cosh(\beta x). \end{aligned} \tag{34}$$

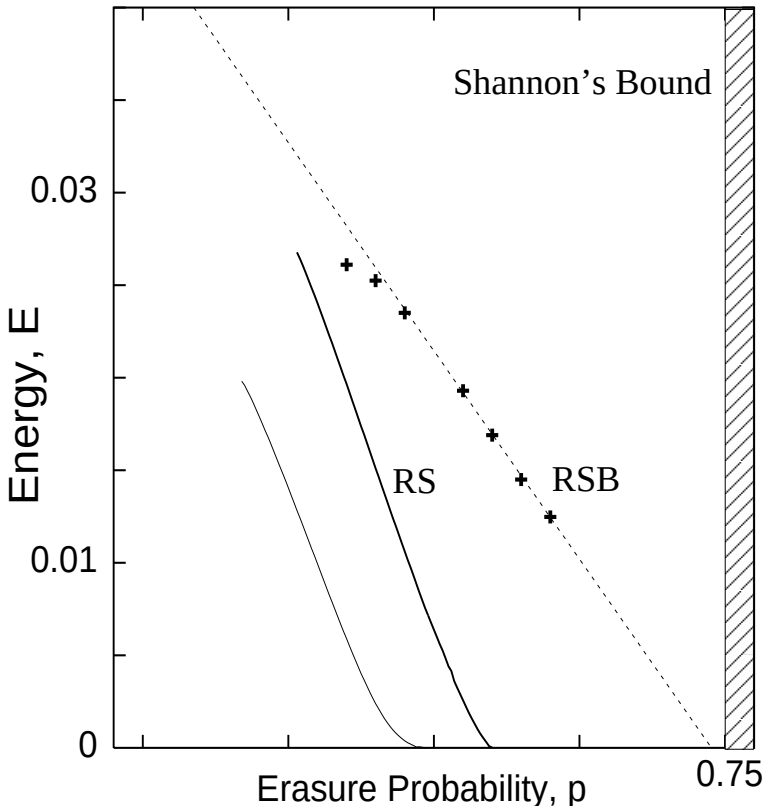

FIG. 13: The RS and RSB Energy as a function of the Erasure probability. The Shannon bound corresponding to the rate $R = 1/4$ being $1 - R$. The points (bold crosses) are extrapolated from the physical branch of the complexity at $\Sigma = 0$ and corresponds to the maximum of the free-energy as a function of the RSB parameter μ. The thin line corresponds to the factorized ansätz.

The fourth term can be written as

$$IV \equiv \Delta f_b^{(1)} \; + \; C \log\cosh(\beta J) \\ + \; C(K-1) \int dx \; \pi(x) \log\cosh(\beta x), \tag{35}$$

where we wrote $\Delta f^{(1)} = \Delta f_a^{(1)} + \Delta f_b^{(1)}$ and where the last term in the free-energy expression above is nothing but $\Delta f_a^{(1)}$. It is easy to see that several terms cancels out, together with the first term in equation (33), to obtain equation (8). Similar simplifications and their interpretation were discussed already in the case of the Bethe SG [11].

Appendix B -The RSB equations

Consider the set of coupled equations (14),

$$\pi(x) \; = \; E_\zeta \int \prod_{i=1}^{C-1} d\hat{x}_i \; \hat{\pi}(\hat{x}) \; \delta\Big(x - \sum_{i=1}^{C-1} \hat{x}_i - F\zeta\Big)$$

$$\hat{\pi}(\hat{x}) \; = \; E_J \int \prod_{j=1}^{K-1} dx_j \; \pi(x_j) \; \delta\Big(\hat{x} - u(\{x_j\}, J)\Big). \tag{36}$$

For the case of $K = 2$, with no random bias, corresponding to the Bethe SG problem, let us define the Laplace transform of the conjugated local field distribution as

$$g(\sigma) = \int d\hat{x} \; e^{-\sigma\hat{x}} \hat{\pi}(\hat{x}). \tag{37}$$

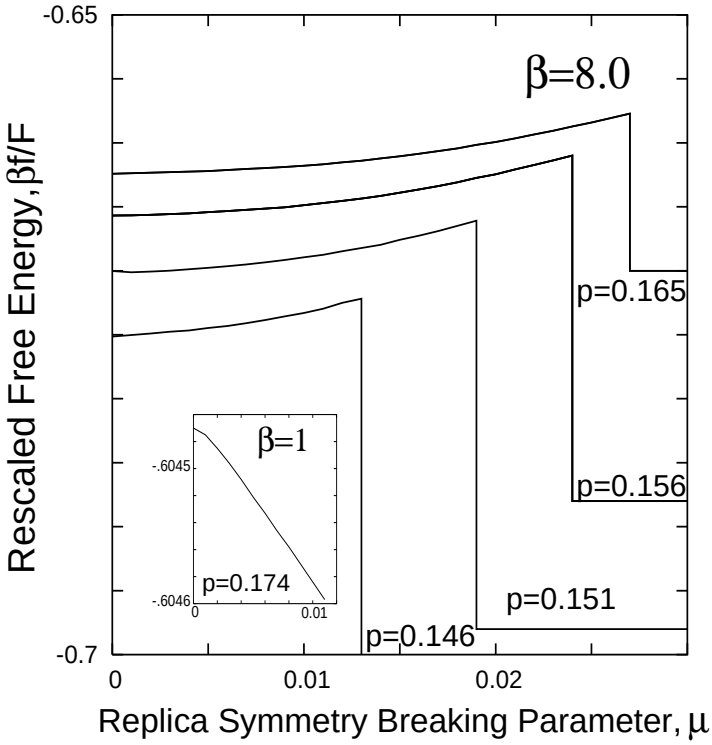

FIG. 14: The Gallager free-energy as a function of the Replica Symmetry Breaking parameter μ for different values of the noise channel p and temperature (the inset showing the free-energy at the Nishimori temperature for a flip rate $p = 0.174$, above the dynamical transition point.)

Substituting the first equation of (36) into the second and then into (37), one finds

$$g(\sigma) = \int ds\ \delta(s + i\sigma)\ E_{J,\zeta} \int \prod_{j=1}^{C-1} d\hat{x}_j\ \hat{\pi}(\hat{x}_j) \times$$
$$\exp\left[\frac{i}{\beta}\tanh^{-1}(\tanh(\beta J)\tanh(\beta\sum_{j=1}^{C-1}\hat{x}_j + \beta F))\right]. \tag{38}$$

which is the expression for the global order parameter found in [5] and corresponds to expression (18) for $K = 2$. The expression for arbitrary K values of the multi-spin interaction simply involves multiple convolutions of the Mottishaw global order parameter. The meaning of the global order parameter (37) can be understood observing that, e.g. in the case of the Bethe SG considered here (in a uniform magnetic field), the partition function is given by [5]

$$\langle Z^n\rangle \equiv Tr_{\{\sigma_o^\alpha\}} \exp\left[\beta F\sum_{\alpha=1}^{n}\sigma_o^\alpha\right][g_m(\sigma_o^\alpha)]^C, \tag{39}$$

where

$$g(\{\sigma_o^\alpha\}) = E_J\Big[Tr_{\{\sigma_1^\alpha\}}(g(\{\sigma_1^\alpha\}))^{C-1}$$
$$\exp\left[\beta J\sum_\alpha \sigma_1^\alpha\sigma_o^\alpha + \beta F\sum_\alpha\sigma_1^\alpha\right]\Big]. \tag{40}$$

The subscript m indicates the dependence of the global order parameter on the sub-shell tree structure. If one is interested in the thermodynamical limit, it is expected that the fixed point of the above recursion determines the equilibrium properties of the system. A delicate point is the choice of the boundary conditions which are well known [11] to play an important role in this problem. The corresponding extension of equation (40) to the case of arbitrary K values has been reported in equation (17).

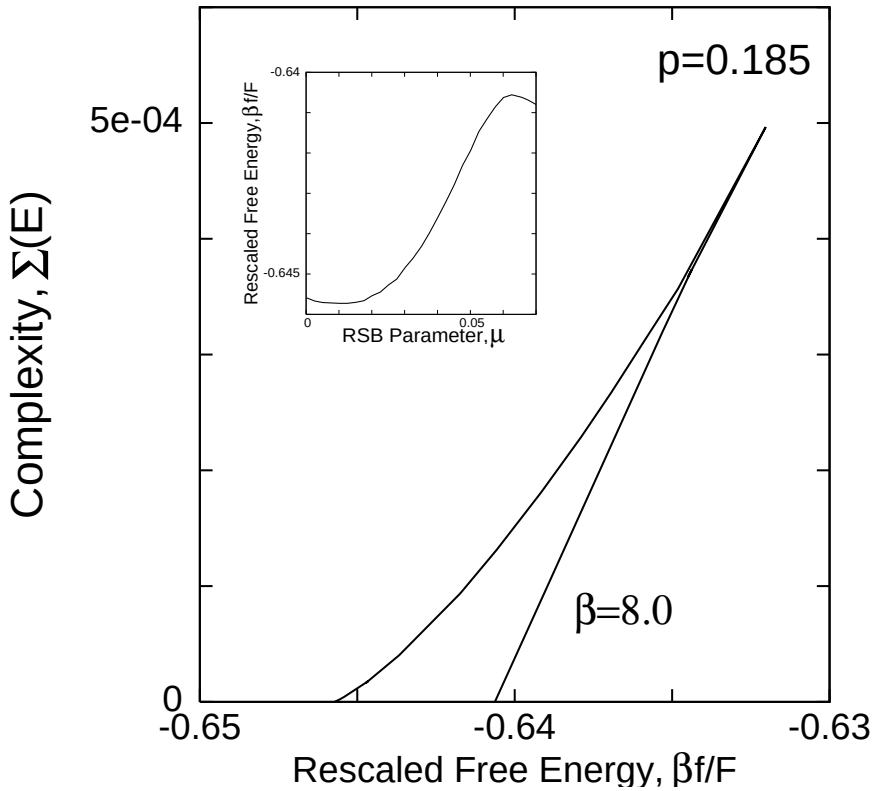

FIG. 15: The Gallager complexity for a BSC noise level of $p = 0.185$, at temperature $\beta = 8.0$, below the Nishimori line. The inset shows the corresponding free-energy as a function of the RSB parameter μ.